Determination and optimization of material parameters of particle-based $LaTiO_2N$ photoelectrodes

Yannick K. Gaudy[1], Stefan Dilger[2], Steve Landsmann[2], Ulrich Aschauer[3], Simone Pokrant[4] and Sophia Haussener[1,*]

[1] École Polytechnique Fédérale de Lausanne, Institute of Mechanical Engineering, Laboratory of Renewable Energy Science and Engineering, 1015 Lausanne, Switzerland
[2] Empa Swiss Federal Laboratories for Materials Science and Technology, Laboratory Materials for Energy Conversion, Überlandstrasse 129, 8600 Dübendorf, Switzerland
[3] University of Bern, Department of Chemistry and Biochemistry, Freiestrasse 3, 3012 Bern
[4] University of Applied Sciences Saarland, Goebenstraße 40, 66117 Saarbrücken,Germany

Abstract

We developed a validated numerical model capable of predicting the photocurrent-voltage characteristics of oxide and oxynitride particle-based photoelectrodes and identifying the critical parameters affecting the performance of those photoelectrodes. We used particle-based $LaTiO_2N$ photoelectrodes as the model system. Two different types of electrodes were studied: $LaTiO_2N$ photoelectrodes with TiO_2 inter-particle connections and the same photoelectrodes with $NiO_x/CoO_x/Co(OH)_2$ co-catalysts and a Ta_2O_5 passivation layer. The necessary material parameters, namely complex refractive index, permittivity, density of states of the conduction and valence bands, charge mobilities, flatband potential, doping concentration, recombination lifetimes, and interfacial hole transfer velocity, were derived by density functional theory calculations, dedicated experiments, and fitting of the numerically determined photocurrent-voltage curves to the measured ones under back-side illumination. The model was validated by comparing its prediction to front-side illumination photocurrent-voltage measurements. A parametric study was then carried out to provide an extensive set of material design guidelines and key parameters for high-performing particle-based $LaTiO_2N$ photoelectrodes. The interfacial hole transfer velocity was identified as the most significant parameter for the performance of $LaTiO_2N$ photoelectrodes.

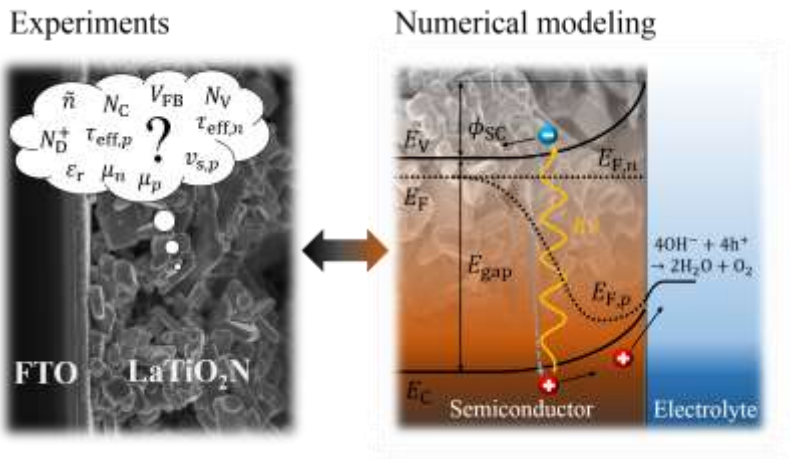

1. Introduction

The direct conversion of solar energy into chemical fuels via photoelectrochemical (PEC) water splitting is a viable route for the production of solar hydrogen[1,2]. Scaled production of solar

*Corresponding author. E-mail address: sophia.haussener@epfl.ch, tel.: +41 21 693 38 78.

hydrogen must be cost competitive with non-renewable hydrogen production (mostly steam reforming of natural gas), which requires scalable PEC approaches that produce hydrogen with high efficiency but at low cost. PEC approaches using particle-based photoelectrodes (PEs), which can be fabricated with simple dip or slurry coating procedures that are already scaled in industrial battery production, can be a route to efficient and economic solar hydrogen. $LaTiO_2N$ (LTON) is a promising PEC material with a suitable bandgap of 2.1eV[3,4] which enables the absorption of visible light up to 590nm. Indeed, highly preforming particle-based LTON PEs with a photocurrent density up to 8.9mA/cm^2 at 1.23V vs RHE were recently reported[5]. However, the various material parameters of particle-based LTON PEs must be determined, and the impact of each parameter on the photocurrent and their underlying multi-physical phenomena must be investigated and understood to further improve the performance of particle-based LTON PEs.

Numerical modelling can help in identifying crucial material, processing, and design challenges for PEs, not accessible and identifiable by experimental investigations. Berger et al. introduced the first 1-dimensional (1D) PEC electrode model for investigating the light absorber's role on the device performance by accounting for the charge transport in the electrolyte and in the semiconductor[6]. This model was developed for homogeneous, thin-film photoabsorber materials and metallic catalysts and was compared to a crystalline-Si PEC cell with Pt as a hydrogen evolution reaction catalyst, two materials with well-known material parameters. These parameters were either taken from literature or assumed (for example, the charge transfer rate constant from the semiconductor to the electrode). Cendula et al.[7] introduced a 1D model capable of describing photocurrent-voltage (I-V) curves and energy band dynamics of photoabsorbers in direct contact with an electrolyte. Their work was based on n-type hematite and p-type cuprous oxide, two known semiconductor materials. However, some material parameters such as the densities of states of the conduction and valence band and the relative permittivity of cuprous oxide were assumed. The 1D numerical model of charge transfer at the semiconductor-catalyst-electrolyte interface by Mills et al. provided the flexibility to account for different types of catalysts (metallic, adaptive, and molecular), and has provided insights into the I-V characteristics of semiconductor-catalyst-solution sytems[8]. Their model was based on semi-classical macroscopic semiconductor physics, similarly to what we use here. They assumed numerous parameters (for example, the hole/electron transfer rate constants) and compared their results to experiments with a n-TiO_2 photoabsorber and IrOx, hydrous $Ni(OH)_2$/NiOOH, and NiOx catalysts. Our previous work with a 1D validated numerical model, accounting for electromagnetic wave propagation (EMW) within the electrolyte and semiconductor and for charge carrier transport and conservation within the semiconductor and at the semiconductor-electrolyte interface, has shown the significant impact of surface lifetimes on the photocurrent for a thin-film GaN photoanode, a well-defined material with known material parameters[9]. It becomes obvious from these early modelling works that the knowledge of the material parameters is key for model accuracy. However, determining the material parameters of many well-known, well-defined materials and films is already a challenge. For this reason, successful models have been mostly limited to classical semiconductor materials such as Si, GaAs, GaInP, TiO_2 or GaN[6,9–12], in monocrystalline and almost defect free thin films. Detailed experimental characterization of these materials has been done for decades, and essential material parameters (e.g. electrical transport properties or electron and hole recombination lifetimes) are well documented in literature[13–16] or in well referenced electronic archives[17]. However, many of the recent materials (e.g. $BiVO_4$[18,19], $SrTiO_3$[20,21] and LTON) used in high performing PEs are complex oxides or oxynitrides. The parameters of these materials are less investigated and also less straight forward to determine since variations in the synthesis procedure induce significant differences in terms of defect density and morphology for the same compound. Transport properties

are especially difficult to assess since the preparation of comparable thin films is not yet possible for some complex oxides and oxynitrides like LTON[22]. This is one of the significant challenges in building a realistic numerical model of particle-based PEs of oxides and oxynitrides.

The second challenge is related to the multi-physical nature of PEs[23,24]. Most of the material parameters are difficult to determine since they depend on multi-physical interactions. It is often not possible to determine them with one dedicated experiment or numerical model. Instead, a combination of experiments and numerical modeling must be used to isolate each physical process with its related parameters. Numerous experiments, such as spectrophotometry, electrochemical impedance spectroscopy (EIS), and conduction measurements, are required and need to be carefully combined with molecular and macroscopic numerical models in order to build a complete model capable of describing the I-V characteristics of oxide and oxynitride PEs.

The third challenge is related to the morphological complexity of particle-based PEs for which a traditional 1D model is not appropriate and a 3D discrete model is not yet practical. In such a complex PE, each photocatalytic particle is almost fully surrounded by an electrolyte enabling the oxygen evolution reaction (OER). The use of a 1D model would reduce this continuous interface to a single one at the model's boundary. Therefore, a 1D model requires to determine an average path for charge transport and conservation which can only be found once all other material parameters are known. In contrast, a 3D-scale model based on the exact morphology can fully capture the physical behavior of particle-based PEs, but the morphological complexity of LTON particles, including nanopores inside and at the surface of particles, introduce considerable computational efforts and require nano-scale transport modeling. Additionally, inter-particle charge transfer mechanism have not been investigated for our PEs. Therefore, it is challenging to develop a model with a simplified morphology that can still capture the physical behavior of LTON particle-based PEs and allows for understanding the interplay of multi-physics processes and identifying key factors in the performance of LTON PEs.

Here, we describe the development of a 2D model which is able to predict the performance of particle-based PEs made of oxynitrides, specifically LTON particles. LTON particle-based PEs were chosen as the model system because of the monocrystallinity of the particles[25], reproducibility by simple dipping procedures[4], and potential for high performance[5]. The 2D PE model accounts for the EMW propagation, charge generation and transport, and semiconductor-electrolyte interface charge transfer. Bulk material parameters, namely the density of states of the valence and conduction bands and the relative permittivity, were calculated by density functional theory (DFT). Consequently, our approach provides a link between the macroscopic and molecular simulation approaches in PEC materials and devices. Additional material parameters, such as spectrally-resolved complex refractive index, charge mobilities, flatband potential and doping concentration, are extracted from dedicated experiments. The numerical model is used in combination with back-side illumination experiments to inversely determine missing material parameters, such as recombination lifetimes and interfacial hole transfer velocity, parameters not accessible experimentally. By doing so, we identify simultaneously the critical parameters affecting the performance of LTON particle-based PEs while showing the predictive character of the model (specifically predicting the I-V curve under front-side illumination). Finally, we provide pathways for the improvement of LTON PEs by identifying the key parameters contributing to performance enhancement.

2. Numerical I-V curve model

The numerical model to predict the I-V characteristics accounts for EMW propagation, charge transport and conservation, and semiconductor-electrolyte interface charge transfer. All equations are presented in detail in our previous work[9]. Here, we only review the equations relevant to key material parameters for the performance of the LTON particle-based PEs.

Model domain and general assumptions - The complex morphology of LTON PEs is simplified by an equivalent homogeneous domain (Fig. 1) relying on two approximations. First, the light absorption model considers the particle-based PEs as a thin film (Fig. 1.b) of the same thickness as the particle-based PEs with a weighting according to the solid-phase density profile along the thickness. Second, the domain for the semiconductor physics was reduced to the dimensions of an average-sized single particle, approximated by a rectangular domain with two semiconductor-electrolyte interfaces, one ohmic contact between LTON and the fluorine-doped tin oxide (FTO) and one insulation interface to account for contacts with upper particles (Fig. 1.c). Only a single particle in direct contact with the FTO is assumed to significantly contribute to the photocurrent. This approximation can be justified by considering that the inter-particle contact introduces a resistance due to the formation of a double Schottky barrier[26,27], reducing the space charge layer (SCL) potential, V_{SCL}, at the semiconductor-electrolyte [28] as given by $V_{\mathrm{SCL}} = V_{\mathrm{a}} - \sum_i^n V_{\mathrm{IPC},i}$, with V_{a} the applied potential, V_{IPC} the potential drop at the inter-particle contact, and n the number of inter-particle contacts the electron goes through. Additionally, the inter-particle contact reduces the effective electron mobility ($1/\mu_{\mathrm{eff},n} = 1/\mu_{\mathrm{b}} + \sum_i^n 1/\mu_{\mathrm{IPC},i}$) as observed for polycrystalline silicon[29,30] or mesoporous TiO_2. In the latter case, it was observed that the electron diffusion coefficient in the mesoporous TiO_2 dropped when the particles were not well sintered leading to poor performance of dye sensitized solar cells[31]. Generally, photoelectrodes containing only one layer of LTON particles have shown equal or even better performance than multilayer particle-based photoelectrodes, pointing to the vital role of the first particle layer for the performance of the PE[4,5].

The dimensions of the approximated particle size, namely 1.42 µm thickness and 0.6µm width, are based on the average dimensions and orientations of particles calculated by a detailed quantitative structural analysis of LTON particle-based PEs utilizing 3D nano-tomography data of the actual electrodes[32]. A particle identification algorithm based on fitting ellipsoids inside LTON particles was applied to focused ion beam scanning electron microscopy (SEM) data. Particle characterization such as nominal sizes of particles were then determined by fitting a log-normal distribution of particle size in *x*, *y*, and *z* directions. The average orientation of particles in all directions was also determined. The length of the model domain is 1.42µm, corresponding to the average particle size of the longest axis of 1.79µm (Fig. S1) and the average orientation angle of 37.4° (Fig. S2), i.e. the angle between the normal of the FTO plan and the direction of the particle in the longest direction. The width of the model domain is 0.6µm, corresponding to the average particle size of the medium and shortest direction.

Radiation absorption - The electron-hole pair generation rate was calculated considering a 2D EMW propagation model with irradiation wavelengths from 400nm to 590nm, corresponding to the spectrum of the solar simulator, up to the bandgap of LTON (2.1eV=590nm). The irradiation was considered as transverse electric field, and therefore, only the out-of-plane electric field was calculated. Bloch-Floquet theory was assumed for the periodicity on both lateral sides of the computational domain with a width of 5µm, ensuring convergence of the model[33,34]. Fig. 1.b depicts the computational domain, the dimensions, and the boundary conditions of the model.

The location-dependent charge carrier generation rate in LTON particle-based PEs was calculated by solving the Maxwell's curl equation[35] for each spectral band of the irradiation for the given spectrally-resolved complex refractive index and the particle density profile. A spectral band of $\Delta\lambda$ = 4nm was carefully chosen to reduce calculation time without losing accuracy of the calculated generation rate. For non-chromatic sources of light, the total generation rate is the spectral integration of the fraction of the absorbed optical power and the energy of the corresponding photon.

EMW propagation was calculated considering the electrolyte (assumed to have the optical properties of water), the FTO glass, and LTON, with the spectral irradiance of the solar simulator Verasol-2 from Oriel and an incident angle of 0° (Fig. S4). The reflection losses at the semiconductor-electrolyte interface can greatly influence the photogeneration efficiency and were accounted for by adding a 2mm-thin layer of water at the back- and the front-side of the PE. The absorption losses due to the electrolyte are negligible since the water extinction coefficient is below $4{\cdot}10^{-6}$ in the visible range[36,37]. Indeed, the same photogenerated current density was calculated using a smaller thickness of the water layer. The spectral complex refractive index, $\tilde{n}$, of LTON is a material parameter required for the numerical model based on EMW propagation and was extracted from spectrophotometry measurements (see section 3).

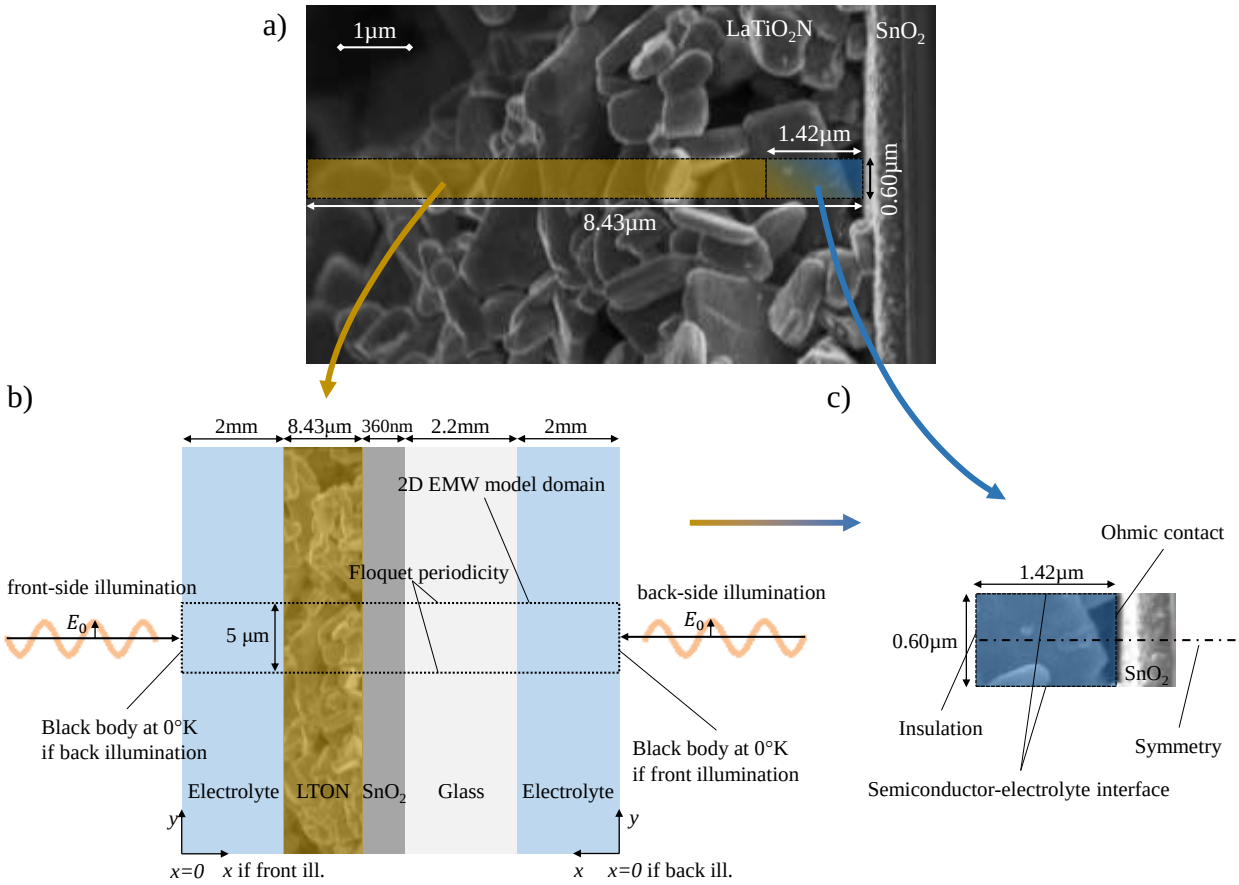

Fig. 1. a) Scanning electron microscopy picture of a LTON particle-based PE and indication of the domain sizes used for the numerical model (yellow for the EMW simulations, blue for the semiconductor physics simulations), b) EMW propagation model domain and boundary conditions, and c) semiconductor physics model domain and boundary conditions. The generation rate calculated with model b) is used as an input in model c).

Charge transport and conservation - The charge transport and conservation were calculated considering a 2D continuum model within the calculation domain. The 2D model, representing an average LTON particle, ensures that the OER can occur along a typical particle surface. The numerical model fully couples the static and the dynamic behavior of charge carriers in the semiconductor. The static behavior was calculated by solving the Poisson's equation[15] with the permittivity and the doping concentration as relevant material parameters. The dynamic behavior of the carriers was calculated by solving the drift-diffusion equation with the electron and hole mobilities as relevant material parameters. The charge carrier density in the semiconductor was determined by the product of the Fermi-Dirac distribution and the density of states of the conduction and valence bands as material parameters. The governing equations were solved at steady-state with a uniform isothermal device temperature of 20°C. The steady-state charge conservation is given by the sum of all recombination and the generation rate, the latter being calculated through the EMW model. Only Shockley–Read–Hall (SRH) recombination was considered and modeled using effective electron and hole lifetimes, given by

$$R_n^{\mathrm{SRH}} = R_p^{\mathrm{SRH}} = \frac{np - n_{\mathrm{i}}^2}{\tau_{\mathrm{eff},p}(n+n_1)+\tau_{\mathrm{eff},n}(p+p_1)}, \tag{1}$$

where $n_{\mathrm{i}} = \sqrt{N_{\mathrm{c}}N_{\mathrm{v}}}e^{-E_{\mathrm{gap}}/(2k_{\mathrm{B}}T)}$ is the intrinsic carrier density, and N_{c} and N_{v} are the conduction and valence band densities of states, respectively. n_1 and p_1 are the electron and hole trap state densities, respectively. The effective electron and hole lifetimes, $\tau_{\mathrm{eff},n/p}$, is a combination of the bulk lifetimes, $\tau_{n/p}$, and the surface lifetimes, $\tau_{\mathrm{s},n/p}$, given by

$$\frac{1}{\tau_{\mathrm{eff},n/p}} = \frac{1}{\tau_{n/p}} + \frac{1}{\tau_{\mathrm{s},n/p}}. \tag{2}$$

We used effective lifetimes to account for both the bulk and the surface recombination, which is in accordance with the general practice of modeling surface recombination[38,39]. This approximation still accurately predicts the I-V characteristics of water-splitting photoelectrodes, as shown in our previous work[9].

The charge transport at the particle-FTO interface was modeled as an ideal ohmic contact. The current density at the semiconductor-electrolyte interface along the side of the particle was determined by using a Schottky contact with the interfacial hole transfer velocity and the flatband potential as relevant material surface parameters. The interfacial hole transfer velocity dictates the kinetics of the oxygen evolution reaction at the semiconductor-electrolyte interface. The hole current, $\boldsymbol{i}_p$, in a Schottky contact (the photocurrent in an n-type semiconductor) is given by

$$\boldsymbol{i}_p \cdot \boldsymbol{n} = q v_{s,p}(p - p_{\mathrm{eq}}), \tag{3}$$

where $\boldsymbol{n}$ is the surface normal, p is the hole concentration at the semiconductor-electrolyte interface, and p_{eq} is the hole concentration at equilibrium. The use of a Schottky contact to describe the charge transfer mechanism at the semiconductor-electrolyte interface simplifies the actual charge transfer mechanisms involved in a photoelectrode with co-catalyst and surface states (SS). A charge carrier can be transferred across different interfaces and paths, such as a direct transfer from the LTON bulk states to the electrolyte, through SS, and/or through co-catalysts. Each path,

with its own kinetic characteristics, is competing with the others. Moreover, SS or co-catalyst might lead to Fermi level pinning, inducing a potential drop not only in the SCL but also in the electrolyte[40]. However, if the band bending due to the semiconductor-electrolyte interface is fully developed and if there is no mass transport limitation from the electrolyte side, the use of a Schottky contact has shown to fit experimental I-V curves well (for example for GaN[9]). We confirmed that an electric field was present at the semiconductor-electrolyte interface by conducting open-circuit voltage measurements for the LTON particle-based PEs (Fig. S5). We also used a highly alkaline solution to ensure that mass transport limits were not present. Furthermore, the Helmholtz layer (HL) capacitance is usually much larger than the SCL capacitance, thus ensuring that the applied potential drops only in the SCL and not in the HL[41,42]. Therefore, the Schottky contact approximation was justified in the present study. Further details and equations related to the Schottky contact mechanism can be found in our previous work[9].

Flatband potential, doping concentration, densities of states, permittivity, charge mobilities, effective lifetimes, and interfacial hole transfer velocity are required material parameters for the charge transport and conservation numerical model and were extracted from molecular numerical model, various experimental measurements, and the inverse analysis (see section 3).

3. Determination of material parameters

Complex refractive index - The complex refractive index, $\tilde{n}=n-ik$, of LTON was extracted from spectrophotometry measurements. Spectral reflectance and transmittance were acquired in an air environment with a UV-3600 Shimadzu UV-VIS-NIR spectrophotometer using an integrating sphere to account for diffuse reflectance and transmittance.

The real part of the complex refractive index, the refractive index, n, of LTON particle-based PEs was determined by using the total reflectance, ρ_m, measured under front-side illumination and using the Fresnel's equations[43] under normal incident, unpolarized light with $n \gg k$, given by

$$n = \frac{n_{air}(\rho_m + 2\sqrt{\rho_m} + 1)}{1-\rho_m} \cong \frac{\sqrt{\rho_m}+1}{1-\sqrt{\rho_m}} \text{ with } n_{air} \cong 1. \quad (4)$$

The imaginary part of the complex refractive index, the extinction coefficient, k, was determined by using the total transmittance, τ_m, and reflectance, ρ_m, measured under back-side illumination. The reflectance measurement was corrected for the absorbance of the FTO glass by $\rho_c = \rho_m + \alpha_{FTO}$. The absorbance of the FTO glass was determined by transmittance and reflectance measurements using $\alpha_{FTO}=1-\rho_{FTO}-\tau_{FTO}$. Following the multiple internal reflections for a single partially transmitting layer with a film thickness much larger than the irradiation wavelength, $D > \lambda$, the reflectance and transmittance are given by[43]

$$\rho_c = \rho_m + \alpha_{FTO} = \rho\left[1 + \frac{(1-\rho)^2\sigma^2}{1-\rho^2\sigma^2}\right] \quad (5)$$

$$\text{and } \tau_m = \frac{\sigma(1-\rho)^2}{1-\rho^2\sigma^2}. \quad (6)$$

where ρ is the light intensity amount reflected, and $1-\rho$ is the amount refracted. σ is the transmitted amount given by $\sigma = e^{-\tau/\cos\theta_i}$ with τ the optical thickness and θ_i the incident angle. The absorption coefficient was assumed to depend on the particle density distribution, $\rho(z)$, along the height, $\alpha(z)=\alpha^{*}\cdot\rho(z)$. The particle density distribution was calculated by a detailed quantitative

structural analysis of LTON particle-based PEs utilizing 3D nano-tomography data of the actual electrodes[32] (Fig. S3). The effective depth, D^*, of particle-based photoelectrode using the particle density distribution is given by

$$\tau = \alpha^* \int_0^D \rho(z)dz = \alpha^* \cdot D^*. \quad (7)$$

By rearranging eqs. (5) to (7) and considering an incident angle of $\theta_i = 0°$, the absorption coefficient, α^*, can be expressed in function of the measured transmittance and the corrected reflectance, given by

$$\alpha^* = -\frac{1}{D^*}\ln\left(\frac{\sqrt{(-\rho_c{}^2+2\rho_c+\tau_m{}^2-1)^2+4\tau_m{}^2}-\rho_c{}^2+2\rho_c+\tau_m{}^2-1}{2\tau_m}\right). \quad (8)$$

Finally, the extinction coefficient depending on the PE's thickness is given by $k(z)=k^*\rho(z)$, where $k^*=\alpha^*\lambda/4/\pi$.

Density of states of the valence and conduction bands, and relative permittivity **-** Assuming parabolic bands in the electronic band structure, the density of states of the valence and conduction bands are given by[44]

$$N_{V/C} = 2\left(\frac{2\pi m^*_{h/e} k_B T}{h^2}\right)^{3/2}. \quad (9)$$

The electron and hole effective masses, $m^*_{h/e}$, of LTON were computed using DFT calculations with the Quantum ESPRESSO[45] package using the PBE[46] exchange-correlation functional with a Hubbard U correction[47] of 3.0 eV applied to the Ti 3d states and using the virtual crystal approximation to describe a $^1/_3$ N $^2/_3$ O disorder on the anion sublattice (for additional computational details, see the supporting information). Based on band structure calculations, we determined the electron and hole effective mass tensors using finite differences with a stencil grid of step size 0.01Bohr^{-1} by means of the EMC utility[48]. For our orthorhombic cell (b is the long axis), we converted the effective masses in all direction into conduction effective masses via

$$m^*_{cond} = 3\left(\frac{1}{m_a}+\frac{1}{m_b}+\frac{1}{m_c}\right)^{-1}. \quad (10)$$

The permittivity of LTON was computed using functional perturbation theory, considering both electronic and ionic contributions.

Flatband potential and doping concentration **-** The flatband potential and the doping concentration were determined by EIS and Mott-Schottky analysis of LTON PEs. The Mott-Schottky plot of LTON PEs using only a capacitance showed a high frequency dispersion (Fig. S6). This frequency dispersion is commonly found in practical electrodes and is attributed to various physico-chemical phenomena, such as surface roughness, surface defects, local charge inhomogeneity, absorbed species, different phase region, variations in composition and stoichiometry, doping inhomogeneity, dielectric relaxation, electric double layer, and deep donor levels [49–51].

Frequency-independent Mott-Schottky plots using Mott-Schottky theory[44,50] can be obtained by using a constant phase element (CPE) combined with the appropriate EIS model. Zoltowski suggested using the following admittance of the CPE[52]:

$$Y_{\mathrm{CPE}} = Y_0(i\omega)^{\alpha}. \quad (11)$$

where Y_0(F·s$^{\alpha-1}$) and α are the frequency independent parameters of the CPE ($0 \leq \alpha \leq 1$), and ω the angular frequency. Y_0 cannot be approximated as a capacitance since a small deviation of α from 1 would lead to large error in the capacitance[51], and Y_0 does not have the unit of a capacitance as mentioned by Zoltowski[52]. The capacitance without any frequency dispersion is obtained from Y_0 and the related resistance, R [49,53], given by

$$C = \frac{(R \cdot Y_0)^{1/\alpha}}{R}. \quad (12)$$

The model for EIS fitting and for determining the flatband potentials and doping concentrations of the best-LTON PEs is depicted in Fig. 4. LTON PEs with co-catalysts were used for the impedance analysis instead of LTON without co-catalysts due to better performance and more reliable results. R_s in the equivalent circuit model denotes a series resistance of the electrolyte and the semiconductor. R_{sc} and CPE_{sc} denote the resistance and the CPE in the SCL. R_{ss} and CPE_{ss} denote the resistance and the CPE caused by SS at the semiconductor-electrolyte interface. This equivalent circuit is usually used for a semiconductor-electrolyte interface with species adsorption at the interface[50] and was previously used for n-type GaN[54].
The model was fitted to a frequency range of 2-16kHz to 50Hz to avoid the slow diffusion component, which is not related to the SCL capacitance[54]. The varying upper frequency limit is due to an abrupt change in the impedance spectra of the best-LTON PEs appearing in all our electrodes at a frequency of 10kHz at 0.12V vs reversible hydrogen electrode (RHE) (Fig. S7). The flatband potential is often determined using the Mott-Schottky equation, which requires that the HL capacitance is much larger that the SCL capacitance. Since the HL capacitance is unknown, the flatband potential is reported without considering any potential shift due to the HL capacitance, in accordance with the general practice[49].

Electron and hole mobilities **-** The conductivity of LTON particle-based PE was measured by 4-point probes with a sourcemeter (Keithley 2450). The mobilities of electron and holes are estimated by conductivity measurements and using the DFT-calculated effective mass of electrons and holes. The conductivity, σ, of a semiconductor material is given by

$$\sigma = q(n\mu_n + p\mu_p), \quad (13)$$

where n and p are the electron and hole densities. μ_n and μ_p are the electron and hole mobilities. Since LTON is naturally a n-type semiconductor material, the hole density in the material is negligible compared to the electron density. Consequently, the hole density term in the conductivity equation (eq. (13)) was neglected. The charge density in the bulk of the semiconductor was assumed to be zero, hence $n \approx N_D^+$, and the electron mobility is given as $\mu_n = \sigma/(qN_D^+)$. By assuming that the average scattering time of electrons and holes is equal, the hole mobility is calculated by

$$\mu_p = \mu_n \frac{m_e^*}{m_h^*}. \quad (14)$$

Electron and hole effective lifetimes and interfacial hole transfer velocity **-** The interfacial hole transfer velocity and effective lifetimes (combination of surface lifetimes at the semiconductor-electrolyte interface, inter-particle contact, and bulk lifetimes) are difficult to access experimentally. Here, we used an inverse analysis for their determination. First, we measured I-V curves under back- and front-side illumination and provided experimental error bars. Then, we applied our inverse analysis which consisted in varying these parameters until the numerical I-V curves fitted the experimental I-V curves under back-side illumination within the error bars. Once, a parameter had been determined under back-side illumination, the numerical photocurrent under front-side illumination was calculated and compared with the corresponding measurement. If the numerical photocurrent under front-side illumination followed the experimental one, the determined parameter was approved, and the model was considered validated and of predictive character. Finally, the exact value of the parameter was determined by minimizing the R-square value of the numerical fitting to the averaged experimental I-V curve above 1V vs RHE under front-side illumination.

4. Experimental section

Photoelectrode preparation and characterization **-** Two types of LTON PEs were prepared following the procedure of Landsmann et al.[4]: best-LTON with multiple coating processes and bare-LTON with a single dipping procedure. In both configurations, the LTON PEs were fabricated using LTON suspended particles deposited on a FTO glass substrate by electrophoretic deposition. Subsequently, the LTON PEs were dipped in an ethanol solution of $Ti(OEt)_4$ and then annealed under a NH_3 flow. This last process ensures ohmic contact between the LTON particles and the FTO glass substrate. These electrodes were called bare-LTON PEs. Best-LTON PEs were obtained by additional dipping of the electrodes firstly in an ethanol solution of $Ta(OEt)_4$ followed by annealing under NH_3 flow to form a passivation layer of Ta_2O_5. NiO_x co-catalysts were then deposited by dipping the electrode in an ethanol solution of $Ni(NO_3)_2$ and subsequently annealed in normal air environment. A similar procedure was used to deposit the CoO_x co-catalyst. Finally, the $Co(OH)_2$ co-catalyst was also deposited by a dipping procedure. SEM images of the electrodes were acquired with a FEI NovaNanoSEM using a through-the lens detector at 5 kV acceleration voltage.

The thickness of the PEs were determined by taking the average thickness along 1µm of the PEs, measured by profilometry using a Bruker DektakX with a 60° tip and an applied contact weight of 1mg. The best-LTON PEs have an average thickness of 8.43µm, and the bare-LTON PEs have an average thickness of 5.51µm. All LTON PEs in this work have an illuminated surface area of $1\pm0.3 cm^2$.

Photoelectrochemical measurements **-** Photoelectrochemical experiments were conducted in a three-electrode setup to refer the potential of our measurements to the RHE. The electrodes were connected to a potentiostat (Bio-Logic VSP-300 controlled by the EC-lab software) for I-V curve measurements and EIS measurements. The reference electrode was Ag/AgCl (sat. KCl), and the counter electrode was Pt. The aqueous electrolyte solutions used were 0.1M Na_2SO_4 and NaOH at pH= 13.2±0.2. The sample was illuminated by the solar simulator VeraSol-2 from Oriel corresponding to AM1.5G in the visible and near-infrared region (400-1100nm) with a light

irradiance of 76±3 mW/cm^2 (Fig. S4). The PEs were measured under front-side illumination with the irradiance transmitted through the electrolyte and absorbed by the LTON and under back-side illumination with the irradiance transmitted through the electrolyte and the FTO glass substrate before being absorbed by the LTON (Fig. 1). I-V curves were measured with a potential sweep of 10mV/s in the potential range of 0.5 to 1.5V vs RHE. A small hysteresis could be observed between forward and backward swept voltage even at this low voltage sweep rate. Therefore, the current density was averaged between forward and backward swept voltage. The final I-V curves depicted in this work for best-LTON and bare-LTON under back- and front-side illumination are the measurement averages of eight fresh PEs each to ensure representative results and stable current conditions (LTON corroded in the electrolyte after a few minutes under illumination). The error bars of the experimental I-V curves are the minimum and maximum photocurrent densities measured for the eight PEs. EIS was done under dark conditions at potentials varying from 0 to 0.6V vs RHE and covering a frequency range of 50Hz to 20kHz.

5. Results and discussion

5.1. Determination of material parameters

5.1.1. Optical parameters and photoabsorption

Complex refractive index - The complex refractive index of bulk LTON calculated with eqs. (4) and (8) from transmittance and reflectance measurements are depicted in Fig. 2. The Tauc plot of LTON is given in the supporting information (Fig. S8). The refractive index based on the total reflectance using eq. (4) has a drop below 600nm. This drop can be interpreted as the bandgap value of LTON (600nm ≈ 2.1eV) using the Kubelka-Munk (K-M) transform based on the total reflectance (Fig. S9). It is therefore often used to determine the bandgap of semiconductors, for which transmittance cannot be measured. The complex refractive of the glass substrate and the FTO layer can be found in the supporting information (Figs. S10 and S11).

For validation purposes, the transmittance was numerically simulated using the obtained optical parameters and compared to the experimental one (Fig. S12). The transmittance was also calculated by utilizing Beer-Lambert's law and additionally accounting for reflectance and absorptance of the FTO glass substrate (Fig. S13). The calculated transmittance for both methods was below 2% error compared to the measured transmittance in a spectral range of 400nm to 590nm. This gave us confidence in the accuracy of the extracted complex refractive index of LTON PEs. The model based on Beer-Lambert's law is very efficient and simple compared to EMW propagation model but should be used with care in the UV region where over 3% error in the transmittance under back-side illumination was observed (relative error of 100% at 340nm, Fig. S13.a).

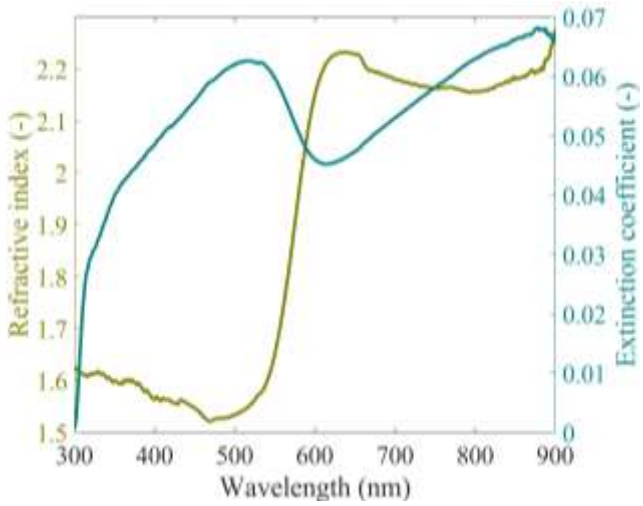

Fig. 2. Complex refractive index of LTON particle-based PE using reflectance and transmittance measurements with an integrating sphere. The refractive index (left *y*-axis) is calculated using Fresnel's equation (eq. (4)) in conjunction with total reflectance measurements. The extinction coefficient (right *y*-axis) is determined using reflectance and transmittance measurements in conjunction with eq. (8) derived by considering multiple internal reflections in a single, partially transmitting thick layer ($D > \lambda$).

Generation rate - The calculated generation rate and photogenerated current density under back- and front-side illumination of the solar simulator is depicted in Fig. 3. Under back-side illumination, the generation rate follows an exponential decay given by the constant extinction coefficient, resulting from a constant density of particles within the first 1.5µm (Fig. S3). The ratio between the front- and back-side illumination photogenerated current density reproduces the experimental front- and back-side photocurrent ratio. The numerical model, considering only the first layer of particles in direct contact with the FTO, is already partially validated, based only on light absorption. As depicted in Fig. 3, the front-side illumination's photogenerated current is more affected by the use of only the first layer of particles. The photogenerated current densities of the front- and back-side illuminations are 0.8mA/cm^2 and 4.4mA/cm^2 respectively.

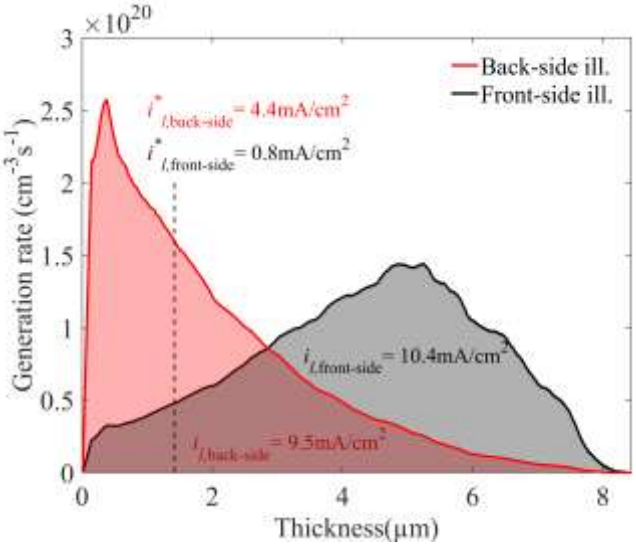

Fig. 3. Generation rate of LTON particle-based PEs under back- and front-side illumination with the AM1.5G solar simulator's spectral irradiance. The integrated photogenerated current density is indicated for PEs of thickness 1.42µm (dashed line) and 8.43µm.

5.1.2 Electronic parameters

Density of states of the valence and conduction bands - For our orthorhombic cell (b is the long axis), the electron effective masses are 0.788, 4.553 and $0.390m_e$ along the a, b and c axes, respectively, whereas the hole effective masses are 0.714, 0.956 and $0.341m_e$, respectively, m_e being the electron mass at rest. We converted these into conduction effective masses via eq. (10), resulting in $0.740m_e$ for the electrons and $0.558m_e$ for the holes. These values agree well with $0.750m_e$ and $0517m_e$ obtained by averaging over conduction effective masses for explicit disorder models[55]. The light holes in oxynitrides can be explained from their electronic structure. While the top of the valence band is N 2p dominated, the Ti 3d dominated bottom of the conduction band is hybridized more with O 2p than N 2p orbitals. Given the stronger covalent Ti-N bond compared to Ti-O, a stronger band dispersion for the N-derived states at the top of the valence band compared to the bottom of the conduction band is expected. Therefore, we observe a lighter mass of the holes compared to the electrons. In pure oxides or nitrides, such an effect would be absent, but we see similar trends for layered Ruddlesden-Popper oxynitrides[56]. The density of states of the valence and conduction bands using eq. (9) are $1.01 \cdot 10^{19} cm^{-3}$ and $1.54 \cdot 10^{19} cm^{-3}$, respectively, at a temperature of 20°C. The electronic band structure of orthorhombic LTON can be found in the supporting information (Fig. S14).

Relative permittivity - The full tensor of the relative permittivity of LTON is given in the supporting information. We converted it to a single value via an effective medium theory[57] and obtained a value of 14.94 without the second order correction and 15.19 with second order corrections. For the macroscopic model, we assumed an approximate relative permittivity of ε_r=15.

Flatband potential and doping concentration – Fig. 4 shows the Mott-Schottky plot for best-LTON PEs in the dark with a resulting flatband potential of 0.1 V vs RHE (in accordance with the work of Feng et al.[58]) and a doping concentration of $7.43 \cdot 10^{17}$ cm^{-3}. The flatband potential of 0.1 V vs RHE is also in accordance with the I-V curve found in a previous paper[58]. A flatband potential of 0.1V vs RHE and a doping concentration of $7.4 \cdot 10^{17} cm^{-3}$ result in a conduction band situated at 0.02V vs RHE, below the hydrogen evolution reaction (HER) potential. However, hydrogen production with LTON particles has been reported by Kasahara et al.[3]. We think that the HER can still occur with the conduction band below the HER potential because these redox systems have a continuous distribution of energy states and not a single discrete state[59]. Nevertheless, this situation will lead to very poor hydrogen production as reported by Kasahara et al. (one order of magnitude lower production of hydrogen than oxygen). The same situation is observed with $BiVO_4$ with a flatband potential of 0.1V vs RHE[60] and the ability to produce hydrogen[61] or $La_5Ti_2CuS_5O_7$ with a valence band above the OER potential[62] and the ability to produce oxygen[63]. The normal surface of the electrode used to calculate the doping concentration with the Mott-Schottky equation[50,64] was $0.79 cm^2$. The active area, A_{active}, was $14.39 cm^2$, utilizing a surface roughness factor of 18.2, obtained from the structural analysis[32] (Table 1). The flatband potential obtained with the best-LTON PEs gives the same result as the one obtained from a Mott-Schottky plot with frequency dispersion (Fig. S6). We can expect to see the effect of SS recombination on the photocurrent up to a potential of 0.6V vs RHE (Fig. 4) and higher, since the onset potential is at 0.9 V vs RHE (Fig. 5). Similar distributions of $1/C_{ss}^2$ have been shown for other semiconductor materials such as TiO_2 in aqueous electrolyte[65].
We obtained a doping concentration variation of $\pm 5 \cdot 10^{17} cm^{-3}$ based on two measurements with newly prepared best-LTON PEs.

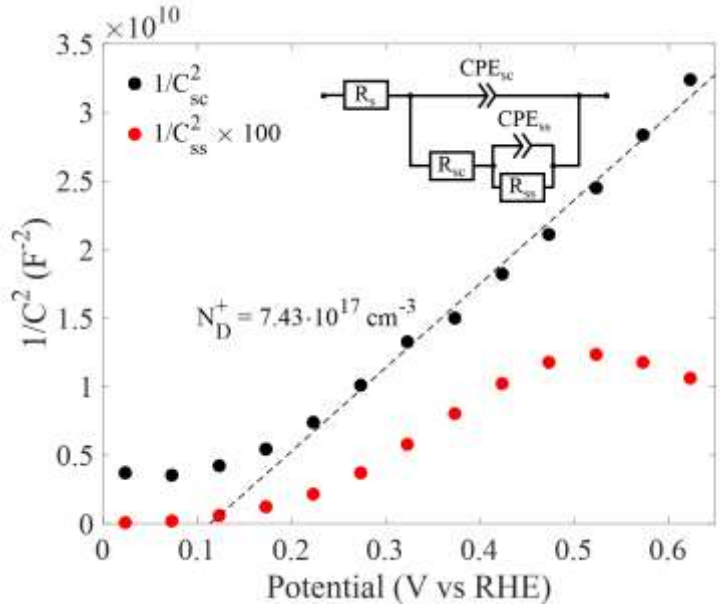

Fig. 4. Frequency-independent Mott-Schottky plots for best-LTON photoelectrodes with the determined doping concentration. The equivalent circuit for the electrochemical impedance analysis is also indicated.

Hole and electron mobilities - The electron mobility of the LTON particle-based PEs is 46 $cm^2V^{-1}s^{-1}$ with a doping concentration of $7.43 \cdot 10^{17}$ cm^{-3} and with a measured conductivity of 5.51 S/cm (eq. (13)). By using the effective masses determined by DFT calculations and using eq. (14), the hole mobility of LTON is 61 $cm^2V^{-1}s^{-1}$.

Effective electron lifetimes - The numerical I-V curves for varying effective electron lifetimes under back- and front-side illumination are presented in Fig. 5, together with the experimentally measured ones. The experimental relative error of the photocurrent is ±17% at 1.23V vs RHE for the best-LTON PEs under back-side illumination and ±30% under front-side illumination. A numerical photocurrent density within the experimental variations above 1V vs RHE under both illuminations' sides is obtained for an electron lifetime of $5 \cdot 10^{-10}$s. We can conclude that our numerical model can reproduce the experimental I-V curves well and is predictive by reproducing the front-side illumination I-V curve. The photocurrent density below 1V vs RHE was not considered for the fitting of the experimental I-V curves since the modeling of the photocurrent in the potential region below 1V vs RHE is highly complex. Indeed, surface recombination is present at low applied potential and any attempt to simulate the photocurrent in this region requires precise knowledge of the surface recombination phenomena with all the related parameters. Thus, this work, in conjunction with state-of-the-art modeling work[7,8], does not address this issue nor reproduces well the I-V curves in the regions where surface recombination occurs (potential below 1V vs. RHE). An in-depth understanding and modeling of surface recombination phenomena at the semiconductor-electrolyte interface would greatly help the community to improve the performance of photoelectrodes but is still missing. The numerical model was also compared to experimental I-V curves under back illumination for different light intensities: 1 sun, 0.1 sun and 0.01 sun. Although some discrepancies between the numerical and the experimental I-V curves occur at a potential between 0.9V to 1.3V vs RHE—most probably due to the surface recombination—the numerical model is able to follow the experimental I-V curves for different light intensities (Fig. S15).

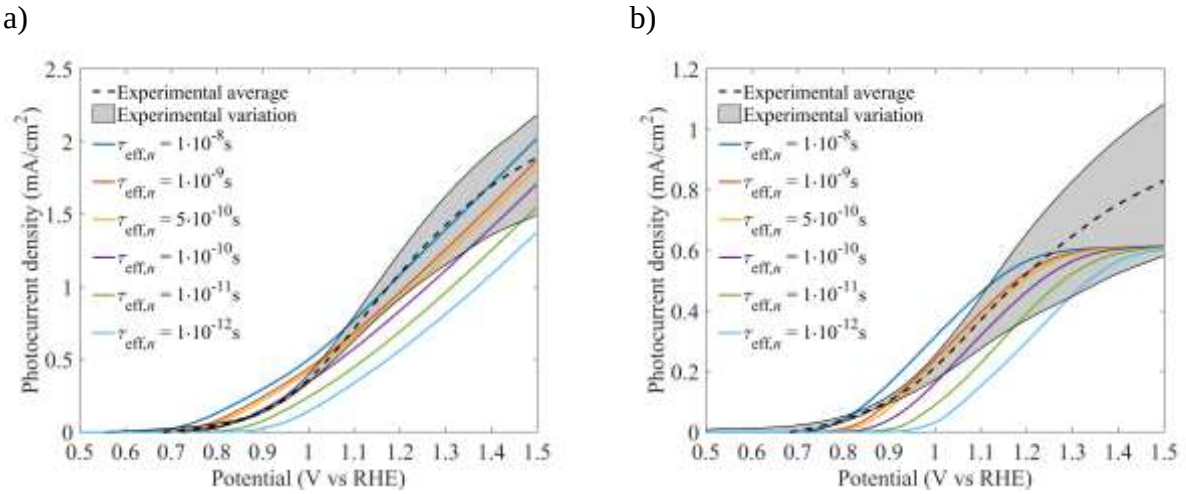

Fig. 5. Numerical and experimental photocurrent-voltage curves of best-LTON under a) back- and b) front-side illumination for varying effective electron lifetimes. The photocurrent density was reduced from 1.18mA/cm^2 to 0.63mA/cm^2 at 1.23V vs RHE when reducing the effective electron lifetime by four orders of magnitude under back-side illumination (from 10ns to 1ps). Under front-side illumination, the photocurrent density was reduced from 0.55 mA/cm^2 to 0.34mA/cm^2 at 1.23V when reducing the effective electron lifetime by four orders of magnitude.

The back-side illumination photocurrent of best-LTON PEs is around 2.5 times higher than the front-side illumination photocurrent at 1.23V vs RHE, although part of the light is absorbed by the FTO glass under back-side illumination and not under front-side illumination. Since electrons are collected at the FTO substrate, electrons generated closer to it have a higher chance to be collected before recombining, leading to a higher photocurrent under back-side illumination. As previously mentioned, we assumed for the modeling that only the first layer of particles in direct contact with the FTO substrate is significantly contributing to the photocurrent. This approximation is supported by the experimental I-V curves (Fig. 5) since the upper particles (not contributing to the photocurrent) are parasitically reducing the light under front-side illumination. This unexpected behavior was attributed in previous work to electron transport limitations due to poor inter-particle conductivity[4,66–68]. The numerical photocurrent reaches saturation already at 1.3V vs RHE while the experimental photocurrent does not show saturation below 1.5V vs RHE (Fig. 5.b). We hypothesize that this discrepancy is caused by the upper particles of the PE starting to contribute to the photocurrent under large applied potential (above 1.3V vs RHE). Such a large applied potential might help to overcome the potential losses appearing at the inter-particle contacts of the upper particles. In the case where there is no potential loss for the upper particles and, thus, the entire thickness of the photoelectrode becomes active, the front-side illumination photocurrent would be larger than the back-side illumination (Fig. S16). This is not observed for our particle-based LTON photoelectrodes. We recognize that in reality a smoother potential drop for the top particles might be experienced, instead of our assumed complete loss of the applied potential above the first layer of particle. Future work will be devoted to investigate this assumption and variations thereof.

Effective hole lifetimes - The impact of effective hole lifetime under back- and front-side illumination on the calculated photocurrents is depicted in Fig. 6, together with the experimentally measured ones. The effective hole lifetime affects both the photocurrent and the onset potential. A

hole lifetime of $5{\cdot}10^{-10}$s gave a photocurrent density within the experimental variation for both illuminations' sides above 1V vs RHE.

a) b)

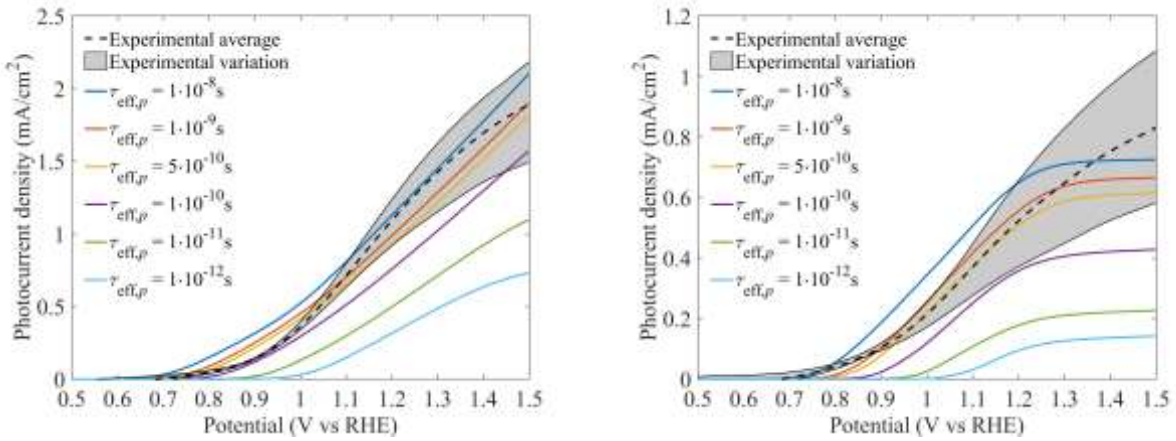

Fig. 6. Numerical and experimental photocurrent-voltage curves of best-LTON under a) back- and b) front-side illumination for varying effective hole lifetimes. The photocurrent density was reduced from 1.01mA/cm^2 to 0.37mA/cm^2 at 1.23V vs RHE when reducing the effective hole lifetime by four orders of magnitude under back-side illumination (from 10ns to 1ps). Under front-side illumination, the photocurrent density was reduced from 0.68 mA/cm^2 to 0.11mA/cm^2 at 1.23V when reducing the effective hole lifetime by four orders of magnitude.

Interfacial hole transfer velocity – The numerical I-V curves for varying interfacial hole transfer velocities under back- and front-side illumination are presented in Fig. 7, together with the experimentally measured ones. The interfacial hole transfer velocity significantly affected the photocurrent under back- and front-side illumination. A hole transfer velocity of $v_{s,p} = 3.5{\cdot}10^{-6}$ cm/s provided a numerical photocurrent within the experimental variation under back-side illumination above 1V vs RHE. The same hole transfer velocity was within the experimental error under front-side illumination.

a) b)

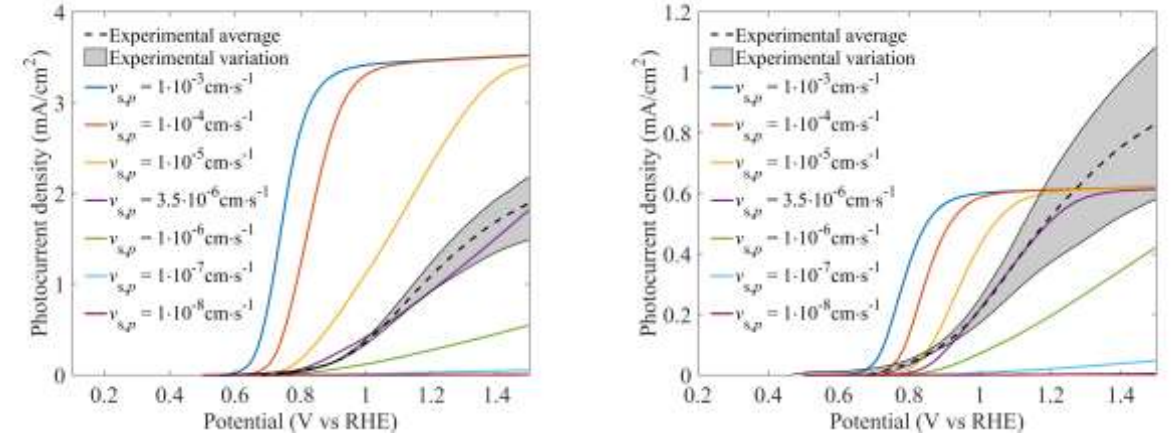

Fig. 7. Numerical and experimental photocurrent-voltage curves of best-LTON PEs under a) back- and b) front-side illumination for varying interfacial hole transfer velocities. The hole transfer velocity was significantly affecting the photocurrent under back-side illumination: a photocurrent of 3.48mA/cm^2 at 1.23V vs RHE with $v_{s,p}$=1·10^{-4}cm·s^{-1} and of 1.01mA/cm^2 with $v_{s,p}$=3.5·10^{-6}cm·s^{-1}. Under front-side illumination, the hole transfer velocity was less affecting the photocurrent since the photocurrent reached almost saturation at 1.23V vs RHE

with $v_{s,p}$=3.5·10^{-6}cm·s^{-1}, a photocurrent density of 0.61mA/cm^2 at 1.23V vs RHE with $v_{s,p}$=1·10^{-4}cm·s^{-1} and of 0.54mA/cm^2 for $v_{s,p}$=3.5·10^{-6}cm·s^{-1}.

All material parameters of LTON particle-based PE used in this work are summarized in Table 1.

Table 1. Material parameters of LTON particle-based PE determined by dedicated experiments (Mott-Schottky analysis and conductivity measurements), DFT calculations, and inverse analysis.

Literature		Band gap, E_{gap}	2.1eV[3,4,66,69–72]
		Electron affinity, χ	4.3eV[71]
Mott-Schottky analysis		Flatband potential, V_{FB}	0.1V vs RHE
		Donor concentration, N_{D}^{+}	$7.43 \cdot 10^{17}$ cm^{-3}
DFT calculation		Relative permittivity, ε_{r}	15
		Effective mass of electron, m_{e}^{*}	0.74
		Effective mass of holes, m_{h}^{*}	0.558
		Density of states of the conduction band, N_{C}	$1.54 \cdot 10^{19}$ cm^{-3}
		Density of states of the valence band, N_{V}	$1.01 \cdot 10^{19}$ cm^{-3}
Conductivity measurements + DFT calculation		Electron mobility, μ_n	46 cm^{2}V^{-1}s^{-1}
		Hole mobility, μ_p	61 cm^{2}V^{-1}s^{-1}
Inverse analysis	Best-LTON	Electron effective lifetime, $\tau_{\mathrm{eff},n}$	$5 \cdot 10^{-10}$ s
	Bare-LTON	Electron effective lifetime, $\tau_{\mathrm{eff},n}$	$1 \cdot 10^{-11}$ s
	Best-LTON	Hole effective lifetime, $\tau_{\mathrm{eff},p}$	$5 \cdot 10^{-10}$ s
	Bare-LTON	Hole effective lifetime, $\tau_{\mathrm{eff,p}}$	$1 \cdot 10^{-11}$ s
	Best-LTON	Interfacial hole transfer velocity, $v_{\mathrm{s},p}$	$3.5 \cdot 10^{-8}$m $\cdot$ s^{-1}
	Bare-LTON	Interfacial hole transfer velocity, $v_{\mathrm{s},p}$	$8.2 \cdot 10^{-9}$m $\cdot$ s^{-1}
Quantitative structural analysis		Height of model domain, d	1.42µm[32]
		Width of model domain, W	0.6µm[32]
		Surface roughness factor, r	18.2[32]
Assumption		Interfacial electron transfer velocity, $v_{\mathrm{s},n}$	$1 \cdot 10^{-12}$ m $\cdot$ s^{-1}*

***An interfacial electron transfer velocity of 1·10^{-12}m/s is assumed to avoid having the back reaction of oxygen reduction.**

5.2 Identifying key material parameters

Interfacial hole transfer velocity - The interfacial hole transfer velocity is highly affecting the performance of the particle-based LTON PEs, as depicted in Fig. 7.a. Indeed, we observed a potential photocurrent increase of 2.3mA/cm^2 at 1.23V vs RHE compared to our current experimental results when increasing the interfacial hole transfer velocity under back-side illumination by a factor of 10. Similar trends were observed for photocurrent densities under front-side illumination, although the improvement was limited to 0.07mA/cm^2 at 1.23V vs RHE (Fig. 7.b). The interfacial hole transfer velocity also reduces the onset potential since it reduces the recombination rate and, thus, the need of a higher band bending at the semiconductor-electrolyte interface. Therefore, less applied potential is required to overcome the recombination present in the SCL. The shape of the photocurrent's curve also changes with varying interfacial hole transfer velocity, i.e. decreasing the slope of the photocurrent curve with smaller velocities. The photocurrent density increased from 2.5mA/cm^2 to 3.5mA/cm^2 at 1.23V vs RHE with $v_{s,p}$ increasing from 10^{-5} to 10^{-4} cm/s, respectively. Above a value of $v_{s,p}$ = 1·10^{-4} cm/s, the photocurrent density remained constant at 3.5mA/cm^2 at potentials above 1.23V vs RHE, only the onset potential was improved. The interfacial hole transfer velocity is the parameter affecting most significantly the performance of LTON particle-based PEs in terms of photocurrent and onset potential.

Hole and electron mobilities – Improving the hole mobility from 10 cm^{2}V^{-1}s^{-1} to 500 cm^{2}V^{-1}s^{-1} does not significantly affect the photocurrent density, i.e. it increased the photocurrent by 0.1mA/cm^2 at 1.23V vs RHE, 10% relative increase (Fig. 8). Under back-side illumination, the

impact of the hole mobility was higher, with an increase of 0.22mA/cm^2 at 1.23V vs RHE (37% relative increase) for a hole mobility increase from 10 cm^{2}V^{-1}s^{-1} to 500 cm^{2}V^{-1}s^{-1}. LTON particles have a high hole mobility, 61 cm^{2}V^{-1}s^{-1}, and this is confirmed by the numerical I-V curves within the experimental error bars (Fig. 8). Therefore, the hole mobility is not a limiting parameters for the performance of the PEs and any further improvement of it by, for example, reducing the doping concentration of the material[73] would not lead to any performance improvement of the LTON PEs. The photocurrent was insensitive to variations of the electron mobility (tested for 0.1 cm^{2}V^{-1}s^{-1} to 500 cm^{2}V^{-1}s^{-1}) under both illuminations' sides (Fig. S17). The photocurrent is a hole current and the electrons are only here to balance the hole current under steady-state, but are not the limiting factor. Only if the electron mobility becomes too small would the electrons not be able to balance the hole current, resulting in the photocurrent abruptly dropping to zero. This was the case under front-side illumination for an electron mobility of 0.1 cm^{2}V^{-1}s^{-1} and below.

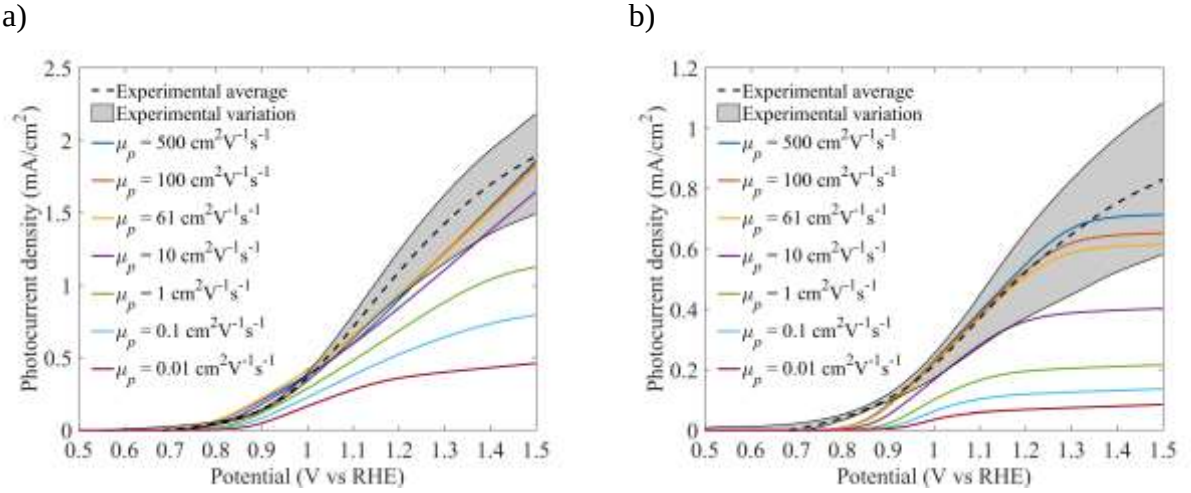

Fig. 8. Numerical and experimental photocurrent-voltage curves of best-LTON under a) back- and b) front-side illumination for varying hole mobilities. The photocurrent density was reduced from 1.02mA/cm^2 to 0.37mA/cm^2 at 1.23V vs RHE when reducing the hole mobility from 500cm^{2}V^{-1}s^{-1} to 0.01 cm^{2}V^{-1}s^{-1}. Under front-side illumination, the photocurrent density was reduced from 0.59 mA/cm^2 to 0.07mA/cm^2 at 1.23V when reducing the hole mobility from 500cm^{2}V^{-1}s^{-1} to 0.01 cm^{2}V^{-1}s^{-1}.

Electron and hole effective lifetimes - Both electron and hole lifetimes are affecting the photocurrent and the onset potential (Fig. 5 andFig. 6). The impact of effective hole lifetime on the photocurrent, however, was greater than for the effective electron lifetime, i.e. the photocurrent increased by 0.5mA/cm^2 at 1.23V vs RHE for an increase of two orders of magnitude in hole lifetime compared to an increase of 0.3mA/cm^2 for an increase of two orders of magnitude in electron lifetime. The impact of the effective hole lifetimes on the photocurrent was less significant compared to the effect of the interfacial hole transfer velocity. The most pronounced effect of increasing effective lifetimes was the downshift of the onset potential for both illumination sides. The applied potential directly changed the band bending at the semiconductor-electrolyte interface, and this bending was reduced with a higher effective electron lifetime.

Doping concentration - Modifying only the doping concentration without changing any other parameters did not influence the performance of LTON PEs under back-side illumination (Fig. S18.a). Under front-side illumination, the photocurrent was slightly increased, 0.1mA/cm^2 at 1.23V vs RHE, by reducing the doping concentration from 10^{19}cm^{-3} to 10^{16}cm^{-3} (Fig. S18.b). Therefore,

the doping concentration must be varied together with other parameters to see an increase in the performance.

5.3 Pathways to improved performance

Properties such as the effective lifetimes, the interfacial hole transfer velocity, and the doping concentration can be modified experimentally to improve the photocurrent. The interfacial hole transfer velocity for best-LTON PEs with CoO_x and CoOH as co-catalysts was still six orders of magnitude smaller than the interfacial hole transfer for n-GaN ($5 \cdot 10^{-2}$ m/s)[9] pointing to the need for co-catalyst improvement. Moreover, the hole transfer velocity of the bare-LTON PE was one order of magnitude smaller than the best-LTON PE, i.e. $8.2 \cdot 10^{-9}$cm/s for bare-LTON and $3.5 \cdot 10^{-8}$cm/s for best-LTON (Table 1 and Fig. S19). Thus, we conclude that either the role of the catalyst is not a truly catalytic one or that the dipping deposition method is not providing a good contact between the catalyst and the photoabsorber. Recently, the deposition of CoOx co-catalyst on LTON particle-based PEs with microwave annealing showed significantly higher photocurrent (8.9mA/cm^2 at 1.23V vs RHE)[5] than the PEs presented in this work. Therefore, different co-catalyst deposition should be investigated in the future to determine if the deposition method is truly the key factor for the performance of LTON particle-based PEs.

The effective lifetimes include surface and bulk lifetimes. The effective lifetimes with a value of 0.5ns for the best-LTON PEs were high compared to other materials with high surface recombination such as GaN[9] (2-3 orders of magnitude higher) but low compared to well-known and efficient material such as Si (effective lifetimes above 1µs[74]). The effective lifetime of the best-LTON PE was improved by one order of magnitude compared to the bare-LTON PEs (Table 1). Thus, surface passivation treatments by the deposition of Ta_2O_5, or surface lifetime improvement by deposition of NiO_x of our best-LTON PEs is confirmed to increase the photocurrent.

The key parameters on the performance of PEs are the effective lifetimes and interfacial hole transfer. These properties were optimized to improve photocurrent densities as depicted in Fig. 9. Additionally, the doping concentration was adapted and optimized accordingly to the new conditions. An internal quantum efficiency (IQE) of 46% (integrated from 400nm to 590nm) was obtained at 1.23V vs RHE by improving the hole transfer velocity from $3.5 \cdot 10^{-6}$cm·s^{-1} to $1 \cdot 10^{-4}$cm·s^{-1}, increasing the hole and electron lifetimes from 5ns to 1ns, and reducing the doping concentration from $7.43 \cdot 10^{17}$cm^{-3} to $1 \cdot 10^{16}$cm^{-3}. Indeed, the photocurrent was increased from 1.2mA/cm^2 to 4.33mA/cm^2 at 1.23V vs RHE, which corresponds to an incident photon-to-current efficiency (IPCE) of 10% by considering the entire solar simulator's spectral irradiance (photon flux current density of 41.56mA/cm^2). An effective lifetime of 1ns corresponds to a pure bulk lifetime with complete removal of surface recombination if we assume a bulk lifetime of 1ns like for GaN[9]. The onset can be reduced to 0.1V vs RHE with a strong photocurrent increase at 0.3V vs RHE by further increasing the hole transfer velocity to 100cm/s. Nevertheless, such a high charge transfer velocity is unlikely to be achieved even with highly performing co-catalysts.

By only increasing the surface properties of LTON particles, we reached an IQE of 40% at 1.23V vs RHE which corresponds to a photocurrent increase of 2.56mA/cm^2, from 1.2mA/cm^2 to 3.76mA/cm^2. This photocurrent density corresponds to an IPCE of 9%, three times larger compared to our current experimental value of 3%.

Although these improvements are important, they are greatly limited by the fact that only the first layer of particles is contributing to the photocurrent. Much higher improvement could be achieved if the entire film thickness of the LTON PEs would contribute to the photocurrent and will be investigated in the future.

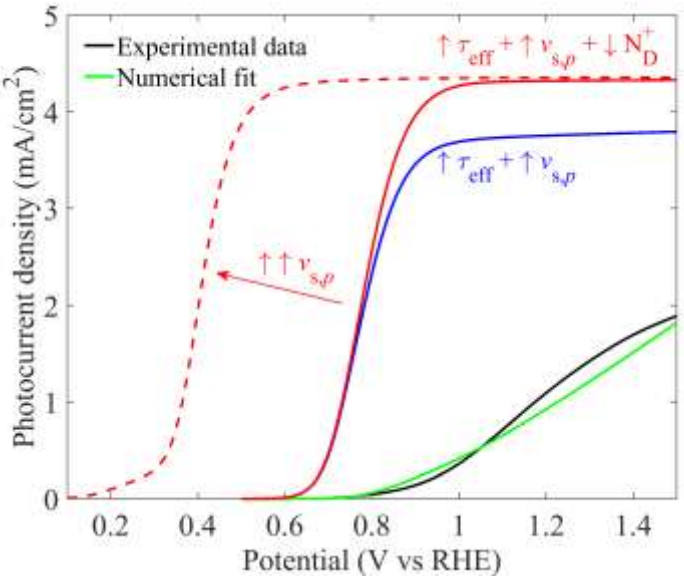

Fig. 9. Numerical and experimental photocurrent-voltage curves of best-LTON under back-side illumination for effective lifetime and interfacial hole transfer velocity optimization (blue line) and for additionally doping concentration optimization (red line). The current IPCE is 3% (black or green line) and is improved to 9% (blue line) by only improving the effective lifetimes of hole and electron from 0.5ns to 1ns and the interfacial hole transfer velocity from $3.5 \cdot 10^{-6}$cm·s^{-1} to 1.10^{-4}cm·s^{-1}. The IPCE can be further improved to an IPCE of 10% by reducing the doping concentration from $7.43 \cdot 10^{17}$cm^{-3} to 1.10^{16}cm^{-3}. The onset potential can be reduced to 0.1V vs RHE by increasing the interfacial hole transfer velocity to 100cm·s^{-1} (red dashed line).

6. Conclusion

We presented an experimental-numerical approach for determining material parameters that are not easily accessible otherwise. We successfully connected macro-scale and molecular-scale modeling with optical, transport, and electrochemical experiments to provide—for the first time—all necessary parameters to build a 2D numerical model capable of predicting the I-V curve of particle-based LTON PEs. Furthermore, this numerical model provides a predictive tool for the performance of morphologically complex, multi-component LTON PEs. It allowed us to identify and to study the impact of key parameters on the photoelectrode's performance in order to deduce material design guidelines for materials scientists and give recommendations for pathways to photoelectrode performance engagements. We found that the interfacial hole transfer velocity was the most important parameter, and its improvement should be prioritized. Indeed, photocurrent density was numerically improved by 2.3mA/cm^2 at 1.23V vs RHE (from 1.2mA/cm^2 to 3.5mA/cm^2) by boosting only the interfacial hole transfer velocity. Further improvements up to a photocurrent of 4.3mA/cm^2 (IPCE of 10%) were achieved by additionally reducing the doping concentration and increasing the effective lifetime.

The numerical model developed in this work can be further used to study numerically the impact of particle size on the photocurrent, which can be modified using different synthesis routes[4], and on particle density, which can vary with the deposition method of particles. Thus, design guidelines on the particle arrangement and size of particle-based PEs can be determined with this model. Furthermore, a numerical model of the inter-particle charge transfer mechanism between LTON particles can be added to the current model to provide additional understandings of particle-based PEs and the role of inter-particle necking that is still not elucidated.

Acknowledgments

This material is based upon work performed with the financial support of Swiss National Science Foundation under Grant #200021_159547. We thank Silvan Suter (EPFL) for providing the quantified data of the microstructure. We thank Carlos G. Morales-Guio (Stanford University) for support and fruitful discussion on EIS. The interaction with Corsin Battaglia (EMPA) is highly appreciated.

References

(1) Pinaud, B. a.; Benck, J. D.; Seitz, L. C.; Forman, A. J.; Chen, Z.; Deutsch, T. G.; James, B. D.; Baum, K. N.; Baum, G. N.; Ardo, S.; et al. Technical and Economic Feasibility of Centralized Facilities for Solar Hydrogen Production via Photocatalysis and Photoelectrochemistry. *Energy Environ. Sci.* **2013**, *6* (7), 1983.

(2) Dumortier, M.; Tembhurne, S.; Haussener, S. Holistic Design Guidelines for Solar Hydrogen Production by Photo-Electrochemical Routes. *Energy Environ. Sci.* **2015**, 3614–3628.

(3) Kasahara, A.; Nukumizu, K.; Hitoki, G.; Takata, T.; Kondo, J. N.; Hara, M.; Kobayashi, H.; Domen, K. Photoreactions on LaTiO2N under Visible Light Irradiation. *J. Phys. Chem. A* **2002**, *106* (29), 6750–6753.

(4) Landsmann, S.; Maegli, A. E.; Trottmann, M.; Battaglia, C.; Weidenkaff, A.; Pokrant, S. Design Guidelines for High-Performance Particle-Based Photoanodes for Water Splitting: Lanthanum Titanium Oxynitride as a Model. *ChemSusChem* **2015**, *8* (20), 3451–3458.

(5) Akiyama, S.; Nakabayashi, M.; Shibata, N.; Minegishi, T.; Asakura, Y.; Abdulla-Al-Mamun, M.; Hisatomi, T.; Nishiyama, H.; Katayama, M.; Yamada, T.; et al. Highly Efficient Water Oxidation Photoanode Made of Surface Modified LaTiO2N Particles. *Small* **2016**, *12* (39), 1–9.

(6) Berger, A.; Newman, J. An Integrated 1-Dimensional Model of a Photoelectrochemical Cell for Water Splitting. *J. Electrochem. Soc.* **2014**, *161* (8), 3328–3340.

(7) Cendula, P.; Tilley, S. D.; Gimenez, S.; Bisquert, J.; Schmid, M.; Grätzel, M.; Schumacher, J. O. Calculation of the Energy Band Diagram of a Photoelectrochemical Water Splitting Cell. *J. Phys. Chem. C* **2014**, *118*, 29599–29607.

(8) Mills, T. J.; Lin, F.; Boettcher, S. W. Theory and Simulations of Electrocatalyst-Coated Semiconductor Electrodes for Solar Water Splitting. *Phys. Rev. Lett.* **2014**, *112* (14), 148304.

(9) Gaudy, Y. K.; Haussener, S. Utilizing Modeling, Experiments, and Statistics for the Analysis of Water-Splitting Photoelectrodes. *J. Mater. Chem. A* **2016**, *4* (8), 3100–3114.

(10) Tembhurne, S.; Haussener, S. Integrated Photo-Electrochemical Solar Fuel Generators under Concentrated Irradiation - I. 2-D Non-Isothermal Multi-Physics Modeling. *J. Electrochem. Soc.* **2016**, *163* (10), H988–H998.

(11) Tembhurne, S.; Haussener, S. Integrated Photo-Electrochemical Solar Fuel Generators under Concentrated Irradiation - II. Thermal Management a Crucial Design Consideration. *J. Electrochem. Soc.* **2016**, *163* (10), H988–H998.

(12) Hankin, A.; Bedoya-Lora, F. E.; Ong, C. K.; Alexander, J. C.; Petter, F.; Kelsall, G. H. From Millimetres to Metres: The Critical Role of Current Density Distributions in Photo-Electrochemical Reactor Design. *Energy Environ. Sci.* **2017**, *10* (1), 346–360.

(13) *Handbook Series on Semicondoor Parameters*; Levinshtein, M., Rumyantsev, S., Shur, M., Eds.; World Scientific: Singapore, 1996.

(14) Adachi, S. *Handbook on Physical Properties of Semiconductors*; Kluwer Academic Publishers: Boston, 2004; Vol. 3: II–VI C.

(15) Sze, S. M.; Ng, K. K. *Physics of Semiconductor Devices*, 3rd ed.; John Wiley & Sons, Inc.: Hoboken, 2007.

(16) Schroder, D. K. *Semiconductor Material and Device Characterization: Third Edition*, 3rd ed.; John Wiley & Sons, Inc.: Hoboken, 2005.

(17) New Semiconductor Materials. Characteristics and Properties http://www.ioffe.rssi.ru/SVA/NSM/Semicond/ (accessed Jul 4, 2016).

(18) Abdi, F. F.; Firet, N.; Van de Krol, R. Efficient BiVO4 Thin Film Photoanodes Modified with Cobalt Phosphate Catalyst and W-Doping. *ChemCatChem* **2013**, *5* (2), 490–496.

(19) Kim, T. W.; Choi, K.-S. Nanoporous BiVO4 Photoanodes with Dual-Layer Oxygen Evolution Catalysts for Solar Water Splitting. *Science (80-.).* **2014**, *343*, 990–994.

(20) Ham, Y.; Hisatomi, T.; Goto, Y.; Moriya, Y.; Sakata, Y.; Yamakata, A.; Kubota, J.; Domen, K. Flux-Mediated Doping of SrTiO3 Photocatalysts for Efficient Overall Water Splitting. *J. Mater. Chem. A* **2016**, *4* (8), 3027–3033.

(21) Zhang, P.; Ochi, T.; Fujitsuka, M.; Kobori, Y.; Majima, T.; Tachikawa, T. Topotactic Epitaxy of SrTiO3 Mesocrystal Superstructures with Anisotropic Construction for Efficient Overall Water Splitting. *Angew. Chemie - Int. Ed.* **2017**, *56* (19), 5299–5303.

(22) Pichler, M.; Si, W.; Haydous, F.; Téllez, H.; Druce, J.; Fabbri, E.; Kazzi, M. El; Döbeli, M.; Ninova, S.; Aschauer, U.; et al. LaTiOxNy Thin Film Model Systems for Photocatalytic Water Splitting: Physicochemical Evolution of the Solid–Liquid Interface and the Role of the Crystallographic Orientation. *Adv. Funct. Mater.* **2017**, *27* (20).

(23) Xiang, C.; Weber, A. Z.; Ardo, S.; Berger, A.; Chen, Y.; Coridan, R.; Fountaine, K. T.; Haussener, S.; Hu, S.; Liu, R.; et al. Modeling, Simulation, and Implementation of Solar-Driven Water-Splitting Devices. *Angew. Chemie Int. Ed.* **2016**, *55* (42), 12974–12988.

(24) Haussener, S.; Hu, S.; Xiang, C.; Weber, A. Z.; Lewis, N. S. Simulations of the Irradiation and Temperature Dependence of the Efficiency of Tandem Photoelectrochemical Water-Splitting Systems. *Energy Environ. Sci.* **2013**, *6* (12), 3605.

(25) Pokrant, S.; Dilger, S.; Landsmann, S. Morphology and Mesopores in Photoelectrochemically Active LaTiO2N Single Crystals. *J. Mater. Res.* **2016**, *31* (11), 1574–1579.

(26) Blatter, G.; Greuter, F. Carrier Transport through Grain Boundaries in Semiconductors. *Phys. Rev. B* **1986**, *33* (6), 3952–3966.

(27) Greuter, F.; Blatter, G. Electrical Properties of Grain Boundaries in Polycrystalline Compound Semiconductors. *Semicond. Sci. Technol.* **1990**, *5*, 111–137.

(28) Warren, S. C.; Voïtchovsky, K.; Dotan, H.; Leroy, C. M.; Cornuz, M.; Stellacci, F.; Hébert,

C.; Rothschild, A.; Grätzel, M. Identifying Champion Nanostructures for Solar Water-Splitting. *Nat. Mater.* **2013**, *12* (9), 842–849.

(29) Levinson, J.; Shepherd, F. R.; Scanlon, P. J.; Westwood, W. D.; Este, G.; Rider, M. Conductivity Behavior in Polycrystalline Semiconductor Thin Film Transistors. *J. Appl. Phys.* **1982**, *53* (2), 1193–1202.

(30) Verlaak, S.; Arkhipov, V.; Heremans, P. Modeling of Transport in Polycrystalline Organic Semiconductor Films. *Appl. Phys. Lett.* **2003**, *82* (5), 745–747.

(31) Huang, F.; Chen, D.; Chen, Y.; Caruso, R. a.; Cheng, Y.-B. Mesoporous Titania Beads for Flexible Dye-Sensitized Solar Cells. *J. Mater. Chem. C* **2014**, *2* (7), 1284.

(32) Suter, S.; Cantoni, M.; Pokrant, S.; Haussener, S. *Linking Morphology and Multi-Physical Transport in Structured Photoelectrodes*; Manuscript in preparation, 2018.

(33) Nicolet, A.; Guenneau, S.; Geuzaine, C.; Zolla, F. Modelling of Electromagnetic Waves in Periodic Media with Finite Elements. *J. Comput. Appl. Math.* **2004**, *168*, 321–329.

(34) Cole, E. A. B. *Mathematical and Numerical Modelling of Heterostructure Semiconductor Devices: From Theory to Programming*, Springer.; 2009.

(35) Pozar, D. M. *Microwave Engineering*, 4th editio.; Wiley, 2012.

(36) Hale, G. M.; Querry, M. R. Optical Constants of Water in the 200-Nm to 200-Um Wavelength Region. *Appl. Opt.* **1973**, *12* (3), 555–563.

(37) Döscher, H.; Geisz, J. F.; Deutsch, T. G.; Turner, J. A. Sunlight Absorption in Water – Efficiency and Design Implications for Photoelectrochemical Devices. *Energy Environ. Sci.* **2014**, *7* (9), 2951–2956.

(38) Gullbinas, K.; Grivickas, V.; P. Mahabadi, H.; Usman, M.; Hallen, A. Surface Recombination Investigation in Thin 4H-SÍC Layers. *Mater. Sci.* **2011**, *17* (2), 119–124.

(39) Sproul, A. B. Dimensionless Solution of the Equation Describing the Effect of Surface Recombination on Carrier Decay in Semiconductors. *J. Appl. Phys.* **1994**, *76* (5), 2851–2854.

(40) Lichterman, M. F.; Hu, S.; Richter, M. H.; Crumlin, E.; Axnanda, S.; Favaro, M.; Drisdell, W. S.; Hussain, Z.; Mayer, T.; Brunschwig, B. S.; et al. Direct Observation of the Energetics at a Semiconductor/Liquid Junction by Operando X-Ray Photoelectron Spectroscopy. *Energy Environ. Sci.* **2015**, *8*, 2409–2416.

(41) Grimes, C. A.; Varghese, O. K.; Ranjan, S. *Light , Water , Hydrogen*; Springer: New York, 2008.

(42) Vanmaekelbergh, D. Direct and Surface State Mediated Electron Transfer at Semiconductor/Electrolyte Junctions—I. A Comparison of Steady-State Results. *Electrochim. Acta* **1997**, *42* (7), 1121–1134.

(43) Siegel, R.; Howell, J. *Thermal Radiation Heat Transfer*, 4th ed.; Bedford, R. H., Ed.; Taylor & Francis: New York, 2002.

(44) van de Krol, R.; Grätzel, M. *Photoelectrochemical Hydrogen Production*; van de Krol, R., Grätzel, M., Eds.; Electronic Materials: Science & Technology; Springer US: Boston, MA, 2012; Vol. 102.

(45) Giannozzi, P.; Baroni, S.; Bonini, N.; Calandra, M.; Car, R.; Cavazzoni, C.; Ceresoli, D.; Chiarotti, G. L.; Cococcioni, M.; Dabo, I.; et al. QUANTUM ESPRESSO: A Modular and Open-Source Software Project for Quantum Simulations of Materials. *J. Phys. Condens. Matter* **2009**, *21* (39), 1–19.

(46) Perdew, J. P.; Burke, K.; Ernzerhof, M. Generalized Gradient Approximation Made Simple. *Phys. Rev. Lett.* **1996**, *77* (3), 3865–3868.

(47) Anisimov, V. I.; Zaanen, J.; Andersen, O. K. Band Theory and Mott Insulators: Hubbard U Instead of Stoner I. *Phys. Rev. B* **1991**, *44* (3), 943–954.

(48) Fonari, A.; Sutton, C. Effective Mass Calculator. **2012**.

(49) Kavan, L.; Tétreault, N.; Moehl, T.; Grätzel, M. Electrochemical Characterization of TiO2 Blocking Layers for Dye- Sensitized Solar Cells. *J. Phys. Chem. C* **2014**, *118*, 16408–16418.

(50) Cesiulis, H.; Tsyntsaru, N.; Ramanavicius, A.; Ragoisha, G. The Study of Thin Films by Electrochemical Impedance Spectroscopy. In *Nanostructures and Thin Films for Multifunctional Applications*; Tiginyanu, I., Topala, P., Ursaki, V., Eds.; Springer, 2016.

(51) Harrington, S. P.; Devine, T. M. Analysis of Electrodes Displaying Frequency Dispersion in Mott-Schottky Tests. *J. Electrochem. Soc.* **2008**, *155*, C381.

(52) Zoltowski, P. On the Electrical Capacitance of Interfaces Exhibiting CPE Behavior. *J. Electroanal. Chem.* **1998**, *443* (1), 149–154.

(53) Hsu, C. H.; Mansfeld, F. Technical Note: Concerning the Conversion of the Constant Phase Element Parameter Y0 into a Capacitance. *Corrosion* **2001**, *57* (9), 747–748.

(54) Ono, M.; Fujii, K.; Ito, T.; Iwaki, Y.; Hirako, A.; Yao, T.; Ohkawa, K. Photoelectrochemical Reaction and H2 Generation at Zero Bias Optimized by Carrier Concentration of N-Type GaN. *J. Chem. Phys.* **2007**, *126* (5), 054708.

(55) Ninova, S.; Aschauer, U. Surface Structure and Anion Order of the Oxynitride LaTiO2N. *J. Mater. Chem. A* **2017**, *00* (001), 1–7.

(56) Bouri, M.; Aschauer, U. Bulk and Surface Properties of the Ruddlesden–Popper Oxynitride Sr2TaO3N. *Phys. Chem. Chem. Phys.* **2018**, *20* (4), 2771–2776.

(57) Stroud, D.; Kazaryan, A. Optical Sum Rules and Effective-Medium Theories for a Polycrystalline Material: Application to a Model for Polypyrrole. *Phys. Rev. B* **1996**, *53* (11), 7076–7084.

(58) Landsmann, S.; Surace, Y.; Trottmann, M.; Dilger, S.; Weidenka, A.; Pokrant, S. Controlled Design of Functional Nano-Coatings: Reduction of Loss Mechanisms in Photoelectrochemical Water Splitting. *ACS Appl. Mater. Interfaces* **2016**, *8*, 12149–12157.

(59) Memming, R. *Semiconductor Electrochemistry*; Wiley-VCH: Weinheim, 2001.

(60) Ma, Y.; Pendlebury, S. R.; Reynal, A.; le Formal, F.; Durrant, J. R. Dynamics of Photogenerated Holes in Undoped BiVO4 Photoanodes for Solar Water Oxidation. *Chem. Sci.* **2014**, *5* (8), 2964.

(61) Xie, M.; Zhang, Z.; Han, W.; Cheng, X.; Li, X.; Xie, E. Efficient Hydrogen Evolution under Visible Light Irradiation over $BiVO_4$ Quantum Dot Decorated Screw-like SnO_2 Nanostructures. *J. Mater. Chem. A* **2017**, *5* (21), 10338–10346.

(62) Nandy, S.; Goto, Y.; Hisatomi, T.; Moriya, Y.; Minegishi, T.; Katayama, M.; Domen, K. Synthesis and Photocatalytic Activity of La5Ti2Cu(S1− x Sex)5O7 Solid Solutions for H 2 Production under Visible Light Irradiation. *ChemPhotoChem* **2017**, *1* (6), 265–272.

(63) Suzuki, T.; Hisatomi, T.; Teramura, K.; Shimodaira, Y.; Kobayashi, H.; Domen, K. A Titanium-Based Oxysulfide Photocatalyst: La5Ti2MS5O7 (M = Ag, Cu) for Water Reduction and Oxidation. *Phys. Chem. Chem. Phys.* **2012**, *14* (44), 15475.

(64) Miller, E. L.; Deangelis, A.; Mallory, S. *Photoelectrochemical Hydrogen Production*; van de Krol, R., Grätzel, M., Eds.; Electronic Materials: Science & Technology; Springer US: Boston, MA, 2012; Vol. 102.

(65) Tomkiewicz, M. The Potential Distribution at the TiO2 Aqueous Electrolyte Interface. *J. Electrochem. Soc.* **1979**, *126* (9), 1505.

(66) Dilger, S.; Landsmann, S.; Trottmann, M.; Pokrant, S. Carbon Containing Conductive Networks in Composite Particle-Based Photoanodes for Solar Water Splitting. *J. Mater. Chem. A* **2016**, *4* (43), 17087–17095.

(67) Feng, J.; Luo, W.; Fang, T.; Lv, H.; Wang, Z.; Gao, J.; Liu, W.; Yu, T.; Li, Z.; Zou, Z. Highly Photo-Responsive LaTiO2N Photoanodes by Improvement of Charge Carrier Transport among Film Particles. *Adv. Funct. Mater.* **2014**, *24* (23), 3535–3542.

(68) Higashi, M.; Domen, K.; Abe, R. Fabrication of Efficient TaON and Ta3N5 Photoanodes for Water Splitting under Visible Light Irradiation. *Energy Environ. Sci.* **2011**, *4* (10), 4138.

(69) Hisatomi, T.; Minegishi, T.; Domen, K. Kinetic Assessment and Numerical Modeling of Photocatalytic Water Splitting toward Efficient Solar Hydrogen Production. *Chem. Soc. Japan* **2012**, *655* (6), 647–655.

(70) Minegishi, T.; Nishimura, N.; Kubota, J.; Domen, K. Photoelectrochemical Properties of LaTiO2N Electrodes Prepared by Particle Transfer for Sunlight-Driven Water Splitting. *Chem. Sci.* **2013**, *4* (3), 1120.

(71) Paven-Thivet, C. Le; Ishikawa, A.; Ziani, A.; Gendre, L. Le; Yoshida, M.; Kubota, J.; Tessier, F.; Domen, K. Photoelectrochemical Properties of Crystalline Perovskite Lanthanum Titanium Oxynitride Films under Visible Light. *J. Phys. Chem. C* **2009**, *113* (15), 6156–6162.

(72) Nishimura, N.; Raphael, B.; Maeda, K.; Le Gendre, L.; Abe, R.; Kubota, J.; Domen, K. Effect of $TiCl_4$ Treatment on the Photoelectrochemical Properties of $LaTiO_2N$ Electrodes for Water Splitting under Visible Light. *Thin Solid Films* **2010**, *518* (20), 5855–5859.

(73) Mnatsakanov, T. T.; Levinshtein, M. E.; Pomortseva, L. I.; Yurkov, S. N.; Simin, G. S.; Khan, M. A. Carrier Mobility Model for GaN. *Solid. State. Electron.* **2003**, *47* (1), 111–115.

(74) Gaubas, E.; Vanhellemont, J. Comparative Study of Carrier Lifetime Dependence on Dopant Concentration in Silicon and Germanium. *J. Electrochem. Soc.* **2007**, *154* (3), H231.